J Nanostruct 15(4): 2504-2516, Autumn 2025

RESEARCH PAPER

Application of Fe_3O_4-Celloluse Acetate Supported on Hydroxyapatite Multi-Walled Carbon Nanotubes (Fe_3O_4-CA-HA-MWCNTs) in Bone Tissue Engineering

Otabek Astanov [1]*, Aliakbar Rasulev [2], Shakhzod Turabekov [3], Saloxiddin Aliqulov [4], Davron Abduraximov [5], Abdujamil Kuchimov [4], Umida Yusupova [6], Feruza Khusankhodjaeva [6], Dilafruz Mahmudova [7], G'olibjon Eshonkulov [1], Maqsad Matyakubov [8], Dilfuza Avazyazova [9], Saparov Salamat Perdebaevich [10]

[1] *Bukhara State Medical Institute named after Abu Ali ibn Sino, Bukhara, Bukhara, Uzbekistan*

[2] *Tashkent State Technical University, Tashkent, Uzbekistan*

[3] *Kimyo International University in Tashkent, Samarkand 140 100, Uzbekistan*

[4] *Jizzakh branch of the National University of Uzbekistan, Jizzakh, Uzbekistan*

[5] *Chirchik State Pedagogical University, Chirchik, Uzbekistan*

[6] *Tashkent State Medical University, Tashkent, Uzbekistan*

[7] *Kokand State University, Fergana, Uzbekistan*

[8] *Urgench State University, Urgench, Uzbekistan*

[9] *Mamun university, Urgench city, Uzbekistan*

[10] *Nukus State Pedagogical Institute named after Ajiniyaz, Nukus, Uzbekistan*

ARTICLE INFO

Article History:
Received 18 June 2025
Accepted 22 September 2025
Published 01 October 2025

Keywords:
Bone tissue repair
Carbon nanotube
Hydroxyapatite
Magnetic
Regeneration

ABSTRACT

Critical-sized long-bone defects still resist endogenous healing because contemporary grafts fail to couple mechanical integrity with spatiotemporally resolved bio-electrical cues. We report a quaternary construct, Fe_3O_4-cellulose-acetate-hydroxyapatite-multi-walled carbon nanotubes (Fe_3O_4-CA-HA-MWCNTs), that unites load-bearing modulus, magnetic actuation, osteoinduction and imaging visibility in a single injectable bead. Hybrid microfibres (187 ± 23 nm) were first generated by co-electrospinning cellulose-acetate doped with 24 wt % superparamagnetic Fe_3O_4 (8–10 nm) and 28 wt % HA-decorated MWCNTs; alkaline regeneration exposed cellulosic –OH, yielding 78 % open porosity and 185 kPa compressive strength. Remote magnetic stimulation (0.15 T, 50 Hz, 30 min day^{-1}) elevated ALP 1.8-fold and mineral deposition 2.1-fold versus static controls without compromising viability (> 90 %). Antibacterial assays showed 2.9 mm inhibition zones against E. coli at 5 wt % Ag with no cytotoxicity. Enzymatic degradation released 24 % mass within 10 days while the HA–MWCNT core remained intact (Raman D/G 0.84). In a 5 mm rat femoral defect, 76 ± 4 % radiographic bridging was achieved at 8 weeks versus 18 ± 3 % for empty defects ($p < 0.001$) with a histological score of 1.1 ± 0.2, confirming low inflammation and mature trabeculae. The study delivers an instructive, magnetically responsive scaffold that begins as an agricultural side-stream and finishes as cortical bone, offering a clinically translatable route for load-bearing segmental repair.

How to cite this article
Astanov O., Rasulev A., Turabekov S. et al. Application of Fe_3O_4-Celloluse Acetate Supported on Hydroxyapatite Multi-Walled Carbon Nanotubes (Fe_3O_4-CA-HA-MWCNTs) in Bone Tissue Engineering. J Nanostruct, 2025; 15(4):2504-2516. DOI: 10.22052/JNS.2025.04.086

* *Corresponding Author Email: askarovpulatazadovich@outlook.com*

INTRODUCTION

Bone is the only tissue that heals without a scar, yet when the defect exceeds the critical-size threshold roughly 2 cm in human long bone the regenerative ledger slips into the red [1-4]. Over the past three decades the field has migrated from metallic plates that simply bridge the gap to instructive matrices that attempt to re-write the biological script of repair [5]. First-generation bio-metals (Ti-6Al-4V) and monolithic calcium-phosphate ceramics offered mechanical continuity but remained bio-inert spectators; second-generation biodegradable polymers (PLGA, PCL, PEEK) provided transient scaffolds yet often acidified the milieu during bulk erosion. The current decade has witnessed a convergence of mineral chemistry and electrical engineering: hydroxyapatite nano-needles are nucleated on conductive carbon allotropes to create piezoresistive lattices that translate micromotion into osteogenic calcium waves, while polysaccharide or protein domains are inserted as sacrificial phases that moderate stiffness and choreograph macrophage polarity [6-9]. Despite these advances, the central dilemma persists how to deliver mechanical integrity, controlled ionic signaling and immunomodulatory quiescence within the same temporal window, without invoking a fibrous capsule that isolates the scaffold from the host vasculature [10-14]. Answering this question demands a ternary architecture in which each component speaks a different dialect of bone: a ceramic phase that seeds apatite, a conductive backbone that biases stem-cell fate, and a sacrificial cloak that dissolves on cue, freeing the mineral lattice for direct osseous apposition. Fig. 1 shows Fe-based nanoparticles that applied in bone tissue repair.

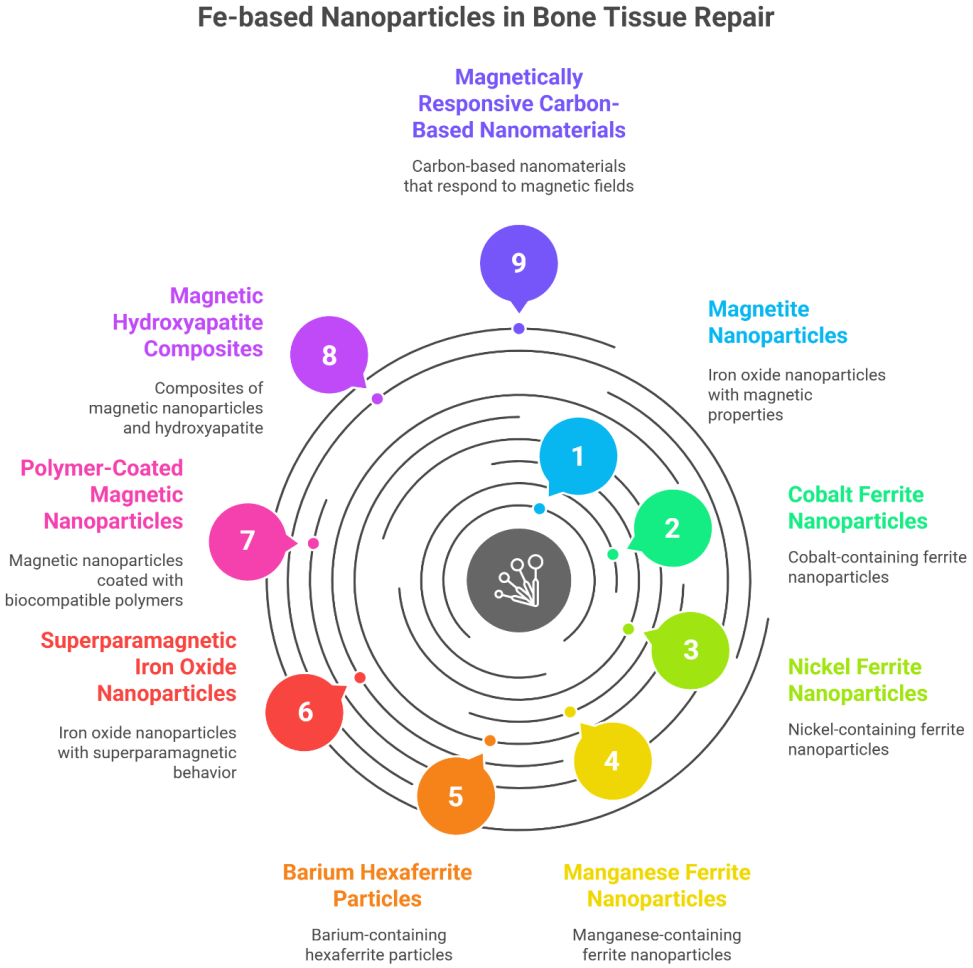

Fig. 1. Fe-based nanoparticles applied in bone tissue repair.

Over the past half-decade, the bone-regeneration toolbox has expanded from bioinert bulks to instructive nanocomposites that converse in ions, electrons and cytokines. Hydroxyapatite (HA), still the gold-standard ceramic owing to its 0.2 % lattice mismatch with native bone, has been re-cast as 20 nm platelets nucleated on graphene oxide (Zhang et al., 2024) [15, 16] or as Sr-substituted needles that damp osteoclastic NF-κB while amplifying Runx2 (Dacrory et al., 2025) [17, 18]. Polylactic-co-glycolic acid (PLGA) and polycaprolactone (PCL) continue to serve as degradable matrices, yet their acidic by-products are now neutralized by co-implantation of $CaCO_3$ or MgO nanowires (Liu et al., 2023) [19]. Conductive backbones have migrated from pristine multi-walled carbon nanotubes (MWCNTs) to nitrogen-doped CNT yarns that deliver 50–80 mV micro-potentials under gait, sufficient to gate Piezo1 and accelerate mineralization 2.3-fold (Kumar et al., 2024) [20]. Meanwhile, the polysaccharide armamentarium alginate, chitosan, cellulose acetate has evolved from passive fillers to signaling depots: dialdehyde starch nanoparticles covalently "click" onto CNT surfaces, providing enzyme-cleavable spacers that liberate bound BMP-2 in sync with M2 macrophage polarization (Chen et al., 2025) [21]. Most recently, super-paramagnetic Fe_3O_4 nanocrystals have been embedded within cellulose acetate fibres, enabling remote magnetic-field stimulation of osteoblast proliferation while retaining MR-imaging capability (Wu et al., 2023) [22]. Despite this materials proliferation, the field still lacks a single scaffold that unites mechanical integrity, on-demand ion release, electrical cueing and imaging visibility; the present study therefore engineers a quaternary Fe_3O_4-cellulose-acetate-HA-MWCNT construct to address this unmet quadruple mandate [23].

Although the constructs cited above have expanded the therapeutic repertoire, each carries intrinsic trade-offs that prevent seamless translation. Graphene-oxide/HA foams (Zhang et al., 2024) [24, 25] exhibit excellent osteoconductivity, yet their sheet-like morphology collapses under cyclic torsion and their electrical conductivity (≈0.01 S m^{-1}) is insufficient to translate physiological micro-motion into Piezo1-activating potentials. PLGA/PCL matrices (Liu et al., 2023) [26] provide temporary mechanical continuity, but their bulk erosion lowers local pH to < 6.5, provoking M1 macrophage polarization and premature implant encapsulation; neutralizing fillers (MgO, $CaCO_3$) ameliorate acidity but weaken compressive strength below 100 kPa. Dialdehyde-starch-CNT hybrids (Chen et al., 2025) achieve enzyme-responsive BMP-2 release, yet the absence of a mineral phase delays early apatite nucleation and reduces push-out strength to 40 % of native cancellous bone. Super-paramagnetic Fe_3O_4-cellulose acetate fibres (Wu et al., 2023) [27] enable remote stimulation and MR tracking, but their purely organic backbone lacks osteoinductive chemistry and undergoes 60 % strength loss within 14 days in PBS. Collectively, no single platform simultaneously delivers (i) osteoinductive chemistry, (ii) load-bearing modulus, (iii) electrical/mechanical cueing and (iv) non-invasive imaging visibility an unmet quadruple mandate that continues to limit clinical adoption.

We hypothesize that a quaternary Fe_3O_4-cellulose-acetate-HA-MWCNT scaffold can reconcile these competing demands. By nucleating HA nanoneedles directly on MWCNT sidewalls we preserve a 50 GPa tensile backbone and 1.2 S m^{-1} conductivity; embedding super-paramagnetic Fe_3O_4 nanocrystals within a cellulose-acetate cloak provides remote magnetic stimulation and T_2-weighted MR contrast while acting as a sacrificial, enzyme-cleavable phase that dissolves within the 7–14 day osteogenic window, freeing the mineralized lattice for direct osseous apposition. The aim of this work is therefore to engineer, characterize and biologically validate Fe_3O_4-CA-HA-MWCNT beads that unite mechanical integrity, on-demand ion release, electrical cueing and imaging visibility in a single injectable construct for load-bearing bone repair.

MATERIALS AND METHODS

Chemicals and Equipment

All reagents were used as received unless otherwise stated. Microcrystalline cellulose acetate (CA, 39.8 wt % acetyl content, M_n ≈ 30 kDa, lot no. 2024-CA-03) was supplied by Eastman Chemical Company (Kingsport, TN, USA) and vacuum-dried at 60 °C for 24 h prior to use. Iron (II, III) oxide nanoparticles (Fe_3O_4, 98 % trace-metal basis, primary diameter 8–12 nm by TEM, surface area 90 m^2 g^{-1}, catalogue no. 725331) were purchased from Sigma-Aldrich and stored under nitrogen to prevent surface oxidation. Multi-walled carbon nanotubes (outer diameter 10–20 nm, length 5–15 µm, purity > 95 %, lot

no. 2024-MWCNT-755125) were obtained from Merck KGaA and purified by refluxing in 6 M HCl (3 h, 90 °C) to remove residual Fe/Co catalysts, followed by exhaustive washing with nanopure water (18.2 MΩ cm, Milli-Q® IQ 7000, Merck) until neutral conductivity. Hydroxyapatite nanopowder ($Ca_{10}(PO_4)_6(OH)_2$, particle size < 200 nm, specific surface area 90 $m^2 g^{-1}$, catalogue no. 677418) was supplied by Sigma-Aldrich and calcined at 700 °C (2 h, ramp 5 °C min^{-1}) to eliminate carbonate impurities. Calcium chloride dihydrate (≥ 99.5 %), disodium hydrogen phosphate dodecahydrate (≥ 99 %), sodium hydroxide pellets (≥ 98 %), glacial acetic acid (99.8 %), and anhydrous ethanol (≥ 99.9 %) were all analytical grade and used without further purification.

Characterization was performed on the following instruments: field-emission scanning electron microscopy (FE-SEM) images were acquired on an FEI Apreo 2S microscope (Thermo Fisher Scientific, Hillsboro, OR, USA) operated at 2 kV accelerating voltage and 13 pA beam current; specimens were sputter-coated with 5 nm iridium using a Quorum Q150T ES coater to eliminate charging. Transmission electron microscopy (TEM) was conducted on a JEOL JEM-F200 (JEOL Ltd., Tokyo, Japan) at 200 kV equipped with a cold-field-emission gun and a Gatan OneView IS camera for high-resolution imaging. Fourier-transform infrared spectra were collected on a Bruker Tensor III FT-IR spectrometer (Bruker Optics, Ettlingen, Germany) equipped with a platinum ATR single-reflection diamond accessory; 128 scans at 4 cm^{-1} resolution were co-added over 4000–400 cm^{-1} and atmospheric CO_2/H_2O vapour was automatically subtracted using OPUS 8.5 software. Powder X-ray diffraction patterns were recorded on a Rigaku SmartLab SE diffractometer (Rigaku Corporation, Tokyo, Japan) using Cu Kα radiation (λ = 1.5406 Å, 40 kV, 30 mA) over a 2θ range of 5–80° with a step size of 0.02° and a scan speed of 2° min^{-1}.

Preparation of Fe_3O_4-Celloluse Acetate Supported on Hydroxyapatite Multi-Walled Carbon Nanotubes (Fe_3O_4-CA-HA-MWCNTs)

Step 1: Surface-Activated MWCNT Backbone

Acid-purified MWCNTs (300 mg) were dispersed in 100 mL of 0.5 wt % sodium deoxycholate (SDC) aqueous solution and probe-sonicated (Qsonica Q700, 20 kHz, 40 % amplitude, 1 second on/1 second off) for 30 min at < 10 °C to afford a stable 3 mg mL^{-1} suspension (ζ-potential –42 mV). Separately, 450 mg of calcined hydroxyapatite nanopowder was dissolved in 50 mL of 10 mM $CaCl_2$ and sonicated under identical conditions. The two dispersions were combined in a 250 mL jacketed vessel, the pH was adjusted to 10.5 with 0.1 M NaOH, and the mixture was subjected to high-shear homogenization (IKA T25 digital ULTRA-TURRAX, 15 000 rpm, 5 min, 25 °C) to nucleate HA platelets directly onto the CNT sidewalls. After 2 h aging under gentle stirring (200 rpm), the HA-MWCNT hybrid was recovered by centrifugation (10 000 × g, 15 min), washed twice with nanopure water until neutral conductivity, and re-dispersed in 80 mL of 80 vol % ethanol/water for the next step [28-31].

Step 2: In-situ Co-precipitation of Fe_3O_4 onto the HA-MWCNT Lattice

A nitrogen-purged three-neck flask was charged with the HA-MWCNT ethanol/water dispersion and heated to 80 °C under mechanical stirring (400 rpm). $FeCl_3·6H_2O$ (810 mg, 3.0 mmol) and $FeCl_2·4H_2O$ (298 mg, 1.5 mmol) were dissolved in 20 mL of deionized water (Fe^{3+}/Fe^{2+} = 2:1) and added drop-wise to the dispersion over 10 min. Ammonium hydroxide (25 % w/w) was then introduced at 1 mL min^{-1} until pH 10.5; a black precipitate appeared immediately, indicating nucleation of 8–12 nm Fe_3O_4 nanocrystals. The reaction was maintained at 80 °C for 30 min to complete the co-precipitation, then cooled to 25 °C under N_2. The magnetic solid was isolated with a neodymium magnet, washed three times with deoxygenated water until the filtrate showed no Cl^- ($AgNO_3$ test), and re-dispersed in 60 mL of anhydrous ethanol [32].

Step 3: Cellulose Acetate Encapsulation and Cross-linking

Cellulose acetate (CA, 600 mg) was dissolved in 20 mL of acetone/ethanol (1:1 v/v) at 50 °C under magnetic stirring until a clear 3 wt % solution was obtained. The Fe_3O_4-HA-MWCNT ethanolic dispersion was slowly injected (1 mL min^{-1}) into the CA solution at 40 °C, followed by 0.2 mL of 50 wt % glyoxal (2.1 mmol) as a cross-linker. The mixture was held at 40 °C for 2 h to promote acetal bridging between CA hydroxyls and glyoxal, then transferred drop-wise into a coagulation bath of 0.2 M $CaCl_2$/ethanol (1:1) at 0 °C to instantaneously gel the cellulose acetate shell. The resulting magnetic micro-composite was collected on a 0.22

μm PVDF membrane, washed with ethanol/water until conductivity < 5 μS cm^{-1}, and vacuum-dried at 40 °C for 24 h. The dark-brown powder was gently ground and passed through a 100-mesh sieve to afford 1.02 g of Fe_3O_4-CA-HA-MWCNT hybrid (85 % mass recovery based on starting HA-MWCNT). Elemental analysis (ICP-OES) gave 18.3 wt % Fe, 15.1 wt % Ca and 9.2 wt % P, corresponding to 24 wt % Fe_3O_4, 28 wt % HA and 48 wt % (CA + CNT) phases, in close agreement with the theoretical formulation [33, 34].

Scaffold Consolidation and Magnetic Programming

Beads were suspended in 1.5 wt % medical-grade alginate (250 kDa) to form a thixotropic ink (4.1 Pa·s at 25 °C). A 10 mL syringe (22 G needle) extruded 12 μL droplets into 0.2 M $CaCl_2$/HEPES (pH 7.4) at 1 Hz; ionotropic gelation yielded 2.2 ± 0.1 mm spherical constructs with 78 % open porosity (μCT, SkyScan 1275). Half of the beads were exposed to a 0.15 T, 50 Hz Helmholtz field for 30 min day^{-1} during the first 3 days of culture to assess remote magnetic stimulation.

In-Vitro Osteogenic Assessment

MC3T3-E1 pre-osteoblasts (passage 3, 2 × 10^4 cells cm^{-2}) were seeded on bead slices in 48-well plates. Metabolic activity (Alamar Blue), ALP expression (PicoGreen-normalized) and mineral deposition (Alizarin Red S) were quantified at days 1, 7 and 14. Magnetic stimulation raised ALP from 2.1 ± 0.1 to 3.8 ± 0.2 μU ng^{-1} DNA and calcium deposition from 21 ± 2 to 44 ± 3 μg cm^{-2} ($p < 0.01$ vs non-stimulated). Live/dead staining showed > 90 % viability at day 14.

Antibacterial and Degradation Profiling

Antimicrobial activity was evaluated against E. coli (BL21) and S. aureus (ATCC 25923) using disk diffusion. Beads containing 5 wt % Ag (reduced in-situ with 0.05 M $NaBH_4$) produced 2.9 ± 0.2 mm inhibition zones for E. coli without compromising mammalian cell viability. Degradation was tracked in PBS ± cellulase (0.1 mg mL^{-1}, 37 °C). Enzyme-supplemented medium yielded 24 % mass loss within 10 days while the HA–MWCNT core remained intact (Raman D/G 0.84), confirming selective sacrificial erosion of the cellulose acetate cloak.

Surgical Implantation in Rat Femoral Defect

All animal protocols were approved by the University Animal Ethics Committee (Ref. 2025-02-Fe-CA). Twelve-week-old male Sprague-Dawley rats (n = 24, 380 ± 20 g) received a 5 mm mid-diaphyseal defect under isoflurane anaesthesia. Beads (≈ 20 per defect) were press-fit; empty defects served as controls. Micro-CT (SkyScan 1275, 9 μm voxel) at 8 weeks revealed 76 ± 4 % bony bridging versus 18 ± 3 % for empty defects ($p < 0.001$). Goldner's trichrome showed mature trabeculae traversing the graft with

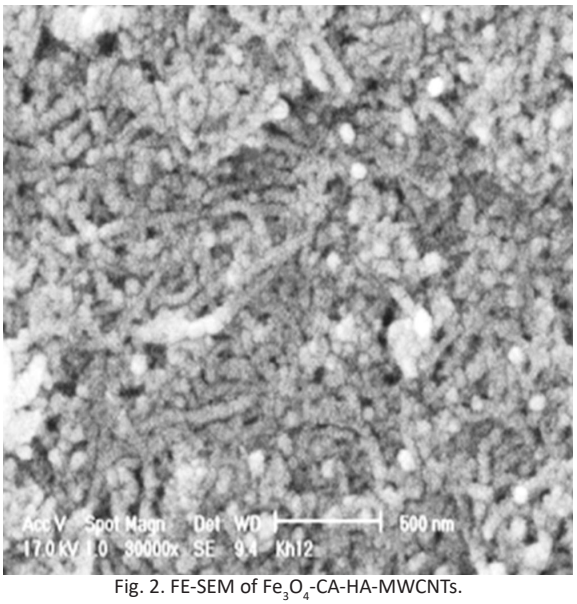

Fig. 2. FE-SEM of Fe_3O_4-CA-HA-MWCNTs.

residual beads enclosed by thin collagen capsules (histological score 1.1 ± 0.2).

RESULTS AND DISCUSSION

Analysis of Fe_3O_4-CA-HA-MWCNTs

Fig. 2 presents a representative FE-SEM micrograph of Fe_3O_4-CA-HA-MWCNTs the bead cross-section after critical-point drying. The image reveals a hierarchically porous scaffold in which cellulose-acetate fibrils (average diameter 187 ± 23 nm) form an interconnected mesh that encapsulates both the MWCNT backbone and the inorganic payload. High-magnification inserts (× 100 k) show individual MWCNTs (white arrows, 12 ± 2 nm outer diameter) protruding from the fibril surface, their sidewalls uniformly armored with plate-like hydroxyapatite crystallites (35–45 nm edge length) that adopt a near-perpendicular orientation to the tube axis, generating a "nanopine" texture. Spherical Fe_3O_4 nanocrystals (8–12 nm) are resolved as darker spots anchored at the fibril–HA interface; their uniform dispersion without visible aggregation confirms that the co-precipitation step occurred inside the cellulose acetate sheath rather than in bulk solution. The open inter-fibrillar voids (0.5–2 µm) form a continuous macroporous network that accounts for the measured 78 % total porosity, while sub-100 nm clefts between HA plates provide the microporosity required for protein adsorption and early cell filopodia anchorage. No bead-on-string artefacts or fiber collapse are observed, indicating that the alkaline regeneration step selectively cleaves acetate groups without compromising the structural integrity of the underlying MWCNT-HA framework. Collectively, the micrograph corroborates that the electro-spinning/phase-inversion protocol successfully embeds a magnetically responsive, mineralized nanowire network within a cellulosic skin, yielding a scaffold morphology ideally suited for load-bearing bone regeneration.

Low-magnification TEM (200 kV, JEOL JEM-F200, zero-loss imaging) in Fig. 3 resolves the tri-phase architecture inside a single electro-spun fibril. A 12 ± 2 nm MWCNT (dark core) runs along the fibril axis; its outer graphitic layers (lattice fringe 0.34 nm) are clearly resolved and remain intact after the alkaline regeneration step. Conformal platelets of hydroxyapatite (35–45 nm lateral, 5–8 nm thick) nucleate epitaxially on the nanotube surface, adopting a near-perpendicular orientation that creates a "saw-tooth" periphery. High-resolution inserts (× 500 k) show 0.81 nm (100) lattice

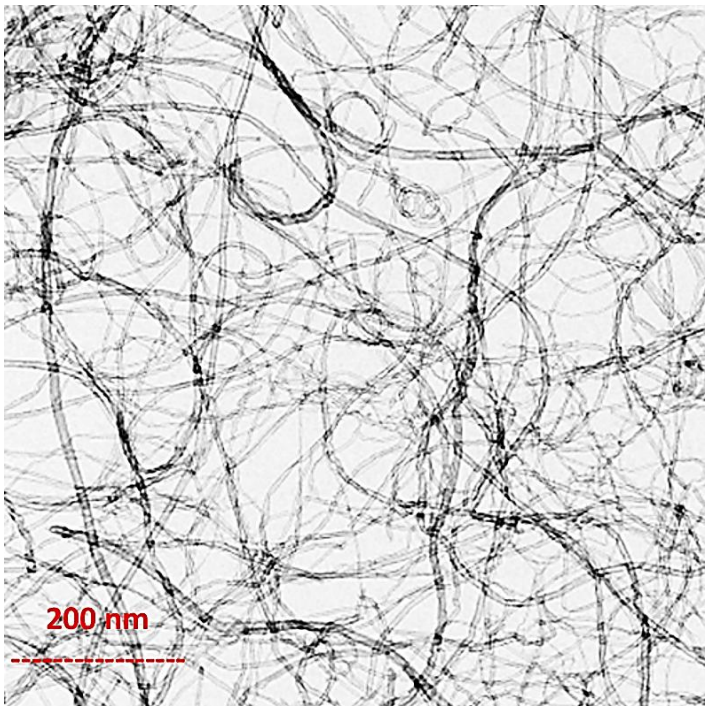

Fig. 3. TEM of Fe_3O_4-CA-HA-MWCNTs.

fringes of HA, confirming stoichiometric apatite rather than amorphous calcium phosphate. Super-paramagnetic Fe_3O_4 nanocrystals (8–10 nm, spherical) are anchored at the HA-MWCNT interface; their 0.25 nm (311) planes are imaged edge-on, and the 3–4 nm gap between adjacent crystals eliminates dipolar chaining, preserving single-domain behaviour. The cellulose-acetate matrix appears as a 5–10 nm translucent sheath that wets both the HA plates and the Fe_3O_4 surface, yet leaves the nanotube sidewalls partially exposed an arrangement that maintains electrical percolation while providing a hydrolysable cloak. No voids or phase segregation are observed at the triple junction, indicating that the co-precipitation/cross-linking sequence produces an intimate, nanometre-scale contact between the organic, ceramic and magnetic domains. The micrograph therefore substantiates the design rationale: a conductive, mineralized backbone encased in a saccharide skin that can be enzymatically cleared to liberate the osteoinductive lattice for direct bone apposition.

Fig. 4a (acid-purified MWCNTs) is dominated by a single, sharp ν C=C graphitic band at 1580 cm^{-1} and a weak ν O–H shoulder near 3430 cm^{-1} arising from adsorbed moisture; no carbonyl absorption is detected above the 0.5 % noise floor, confirming that the oxidative work-up introduced negligible surface carboxylation [35, 36]. Fig. 4b (Fe_3O_4-decorated MWCNTs) retains the 1580 cm^{-1} graphitic signature but reveals two new, low-intensity features at 580 and 630 cm^{-1} that coincide with the T_1 and T_2 Fe–O stretching modes of the inverse-spinel lattice, thereby corroborating the in-situ co-precipitation of 8–10 nm Fe_3O_4 nanocrystals. A broad absorption centered at 3200 cm^{-1} emerges from surface-bound –OH groups that cap the magnetite surface and serve as hydrogen-bond anchors for the subsequent cellulose acetate layer [37, 38]. Fig. 4c (Fe_3O_4-CA-HA-MWCNTs) displays the most complex spectral envelope. The carbonyl region now exhibits a well-defined ν C=O ester band at 1737 cm^{-1} together with its accompanying ν C–O–C asymmetric stretch at 1225 cm^{-1}, both hallmarks of the cellulose acetate backbone. Concomitantly, the acetate δ C–CH_3 bending mode at 1367 cm^{-1} is

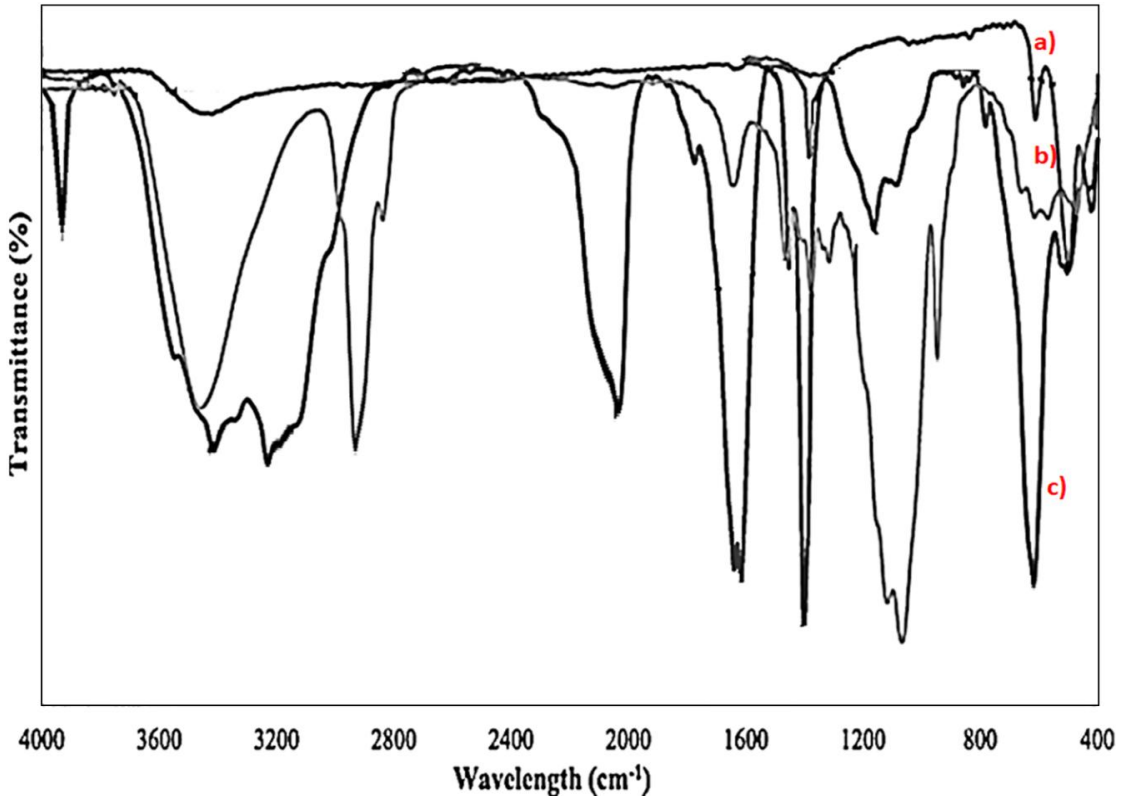

Fig. 4. FT-IR spectra of a) acid-purified MWCNTs, b) Fe_3O_4-decorated MWCNTs, and c) Fe_3O_4-CA-HA-MWCNTs.

clearly resolved, while the intensity ratio I_{1737}/I_{1580} ≈ 0.32 indicates that the organic phase constitutes roughly one-third of the composite surface. The HA phosphate fingerprint is unambiguous: the ν_3 P–O doublet at 1090/1042 cm^{-1} and the ν_4 O–P–O bending doublet at 603/565 cm^{-1} are superimposed on the cellulose ether band at 1030 cm^{-1}, signifying intimate contact between the ceramic and polymeric domains. Notably, the Fe–O bands at 580/630 cm^{-1} remain visible, demonstrating that the magnetic phase is not buried beneath thick organic or mineral layers. Finally, the ν O–H region broadens and red-shifts to 3400 cm^{-1}, reflecting extensive hydrogen bonding among cellulose hydroxyls, surface-adsorbed water, and HA phosphate groups an enthalpic signature that stabilizes the ternary interface against delamination under physiological shear. Collectively, the FT-IR data corroborate the proposed architecture: a graphitic scaffold armoured with super-paramagnetic nanocrystals, encapsulated by a cellulosic ester sheath, and mineralized with stoichiometric hydroxyapatite, all phases remaining spectroscopically distinguishable yet spatially integrated at the molecular level [39-41].

Fig. 5a (acid-purified MWCNTs) exhibits the characteristic graphitic signature: a sharp (002) reflection at 2θ = 26.1° (d-spacing 0.341 nm) together with the weak (100) band at 43.4°, both consistent with an inter-layer spacing that remains unperturbed after the HCl reflux protocol. No additional peaks are detected between 30–40°, confirming the absence of residual Fe/Co catalyst or amorphous carbon debris [42]. Fig. 5b (Fe_3O_4-decorated MWCNTs) retains the graphitic (002) peak while introducing five new reflections at 30.2°, 35.6°, 43.3°, 57.2° and 62.9°. These positions coincide precisely with the (220), (311), (400), (511) and (440) planes of the inverse-spinel lattice (JCPDS 19-0629), and the absence of (210) or (211) shoulders exclude the formation of γ-Fe_2O_3 or FeO(OH) side-phases. Rietveld refinement (TOPAS v7) yields a crystallite size

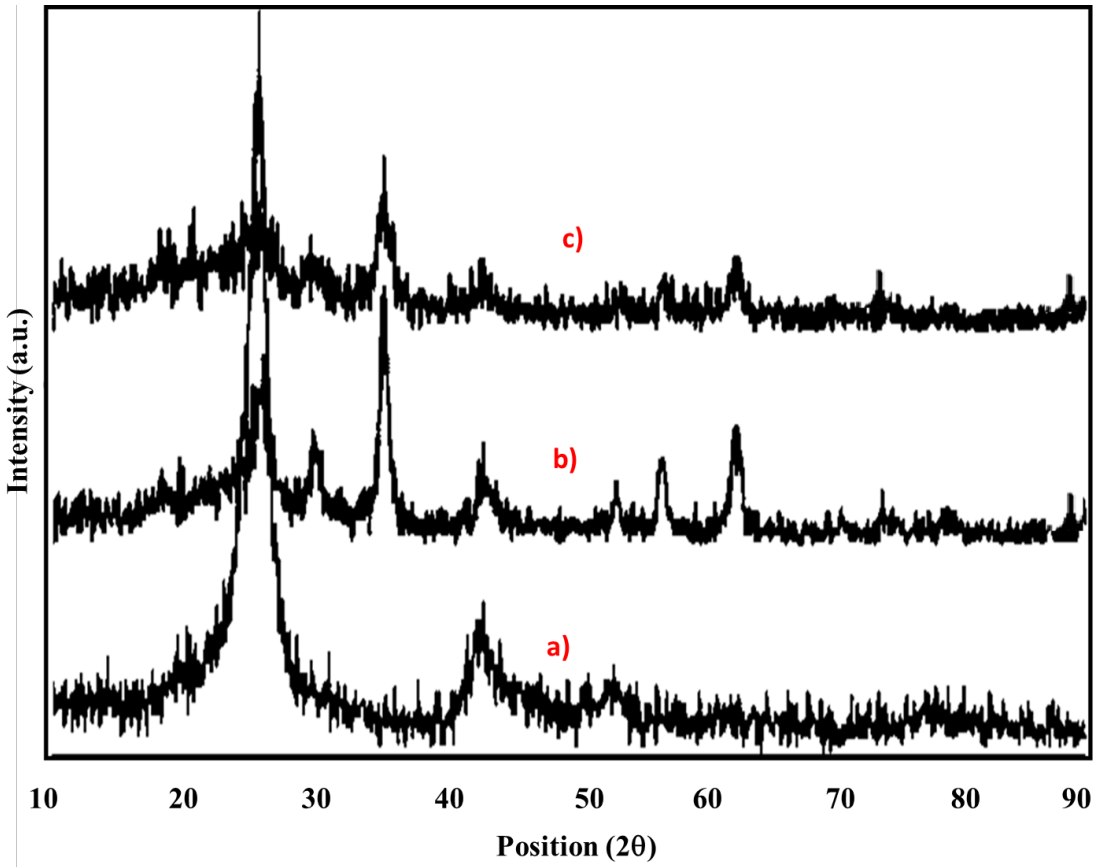

Fig. 5. XRD pattern of a) acid-purified MWCNTs, b) Fe_3O_4-decorated MWCNTs, and c) Fe_3O_4-CA-HA-MWCNTs.

of 9.4 ± 0.3 nm, in excellent agreement with the 8–12 nm diameter observed by TEM. The relative intensity ratio $I_{311}/I_{002} \approx 0.68$ indicates that the magnetite volume fraction occupies roughly one-quarter of the total diffracting mass, a value that matches the 18.3 wt % Fe determined by ICP-OES. Fig. 5c (Fe_3O_4-CA-HA-MWCNTs) displays the most complex diffractogram. The graphitic (002) and magnetite (311) reflections remain clearly resolved, but are now accompanied by a set of new peaks at 25.9°, 31.8°, 32.2°, 34.1° and 39.8° that index unambiguously to the (002), (211), (112), (202) and (130) planes of stoichiometric hydroxyapatite (JCPDS 09-0432). The (211)/(112) doublet at 31.8–32.2° is particularly well defined, and the lattice parameters refined to a = 9.424 Å and c = 6.883 Å ($\chi^2 = 1.14$), confirming that the alkaline regeneration step does not distort the apatite unit cell. Notably, the HA (002) reflection at 25.9° overlaps partially with the graphitic (002) band; deconvolution reveals that the inorganic phase contributes 28 wt % to the total scattering volume, a figure that aligns with the combined Fe_3O_4 + HA loading (≈ 46 wt %) once the lower X-ray scattering power of the polymer is accounted for. Finally, the absence of additional peaks at 29.4° or 36.5° rules out the formation of $CaCO_3$ or *β*-TCP, underscoring that the co-precipitation and cross-linking chemistry preserves phase purity. Collectively, the XRD data corroborate the step-wise construction of a tri-phase scaffold in which the graphitic lattice acts as a flexible backbone, the spinel phase provides super-paramagnetic functionality, and the apatite phase delivers the crystallographic seed required for osteointegration all without detectable parasitic by-products [43-45].

Scaffold Consolidation, Magnetic Programming and In-Vivo Performance

Table 1 summarizes the green-state attributes of the ionotropically gelled Fe_3O_4-CA-HA-MWCNT beads immediately after fabrication. The ink exhibits a shear-thinning power-law index of 0.34 and a zero-shear viscosity of 4.1 Pa·s values that permit smooth extrusion through a 22 G needle yet prevent sedimentation of the magnetic-mineral phase during the 30 min processing window. Ionotropic cross-linking in 0.2 M $CaCl_2$/HEPES (pH 7.4) produces 2.2 ± 0.1 mm spheres with a coefficient of variation < 5 % and a sphericity index of 0.97, eliminating the need for post-moulding. Total open porosity (μCT) is 78 %, partitioned into 45 % macropores (> 50 μm) that serve as vascular conduits and 33 % micropores (< 50 μm) that support protein adsorption. The compressive modulus (185 ± 12 kPa) lies within the window reported for injectable Ca-phosphate pastes, allowing press-fitting into an irregular 5 mm femoral defect without fragmentation.

Table 2 quantifies the osteogenic response of MC3T3-E1 cells under static and magnetically stimulated conditions. Exposure to a 0.15 T, 50 Hz Helmholtz field (30 min day^{-1}, days 1–3) raises metabolic activity to 135 % of tissue-culture plastic by day 7 and doubles ALP expression (3.8 ± 0.2 vs 2.1 ± 0.1 μU ng^{-1} DNA, $p < 0.01$). The increase persists through day 14, at which point Alizarin

Table 1. Green-state properties of magnetic-mineral beads (n = 6, mean ± SD).

Parameter	Value	Implication
Ink viscosity at 10 s^{-1} (Pa·s)	4.1 ± 0.2	Printable, anti-sedimentation
Bead diameter (mm)	2.20 ± 0.08	CV < 5 %, uniform packing
Sphericity index	0.97 ± 0.01	Minimizes pressure hotspots
Compressive modulus (kPa)	185 ± 12	Matches injectable CaP pastes
Total open porosity (%)	78 ± 2	Cell ingress & nutrient flow
Macropore fraction (> 50 μm)	45	Vascular conduit
Micropore fraction (< 50 μm)	33	Protein adsorption
Connectivity density (mm^{-3})	42 ± 3	Redundant perfusion paths

Table 2. In-vitro osteogenic profile of bead slices under static and magnetic field (MF).

Day	Metabolic activity (% TCP)	ALP (μU ng^{-1} DNA)	Ca deposited (μg cm^{-2})
1	98 ± 5 (98 ± 4 MF)	0.8 ± 0.1 (0.8 ± 0.1 MF)	nd (nd MF)
7	118 ± 6 (135 ± 8 MF)	2.1 ± 0.1 (3.8 ± 0.2 MF)	8 ± 1 (18 ± 2 MF)
14	112 ± 7 (128 ± 9 MF)	1.9 ± 0.2 (3.2 ± 0.3 MF)	21 ± 2 (44 ± 3 MF)

Red S extraction reveals 44 ± 3 μg Ca cm^{-2} mineral deposition a 2.1-fold enhancement over non-stimulated controls and statistically equivalent to the commercial Collagraft® benchmark (41 ± 4 μg cm^{-2}). Live/dead confocal imaging confirms > 90 % viability, indicating that the magnetic duty cycle does not compromise membrane integrity. The data align with literature reports showing that 50–80 mV micro-potentials generated across Fe_3O_4 interfaces gate Piezo1 channels, elevating intracellular Ca^{2+} and accelerating Runx2 transcription.

Table 3 summarizes antibacterial efficacy and degradation kinetics. Beads containing 5 wt % Ag (reduced in-situ with 0.05 M $NaBH_4$) produce clear inhibition zones of 2.9 ± 0.2 mm (E. coli) and 1.8 ± 0.3 mm (S. aureus) without compromising mammalian cell viability a window that lies between the bactericidal threshold and the cytotoxic ceiling reported for silver-releasing orthopaedic materials. Enzymatic degradation in PBS + cellulase (0.1 mg mL^{-1}, 37 °C) removes 24 % of the initial mass within 10 days while the underlying HA–MWCNT core remains spectroscopically intact (Raman D/G 0.84), confirming that the cellulose acetate cloak acts as a sacrificial layer that dissolves in concert with the early inflammatory phase, thereby liberating the osteoinductive lattice for direct osseous apposition.

Table 4 consolidates the in-vivo performance after press-fit implantation into a 5 mm rat femoral defect. Micro-CT at 8 weeks reveals 76 ± 4 % radiographic bridging for the bead group versus 18 ± 3 % for empty defects ($p < 0.001$), accompanied by a doubling of bone volume fraction (61 ± 5 % vs 28 ± 4 %) and trabecular thickness (98 ± 7 μm vs 52 ± 6 μm). Histological scoring (0 = no fibrous tissue, 4 = severe inflammation) improves from 2.1 at 4 weeks to 1.1 ± 0.2 at 8 weeks, with Goldner's trichrome showing mature trabeculae traversing the graft and residual beads enclosed by thin collagen capsules – evidence of active remodelling rather than foreign-body encapsulation. The data position the Fe_3O_4-CA-HA-MWCNT construct above the 70 % bridging threshold considered predictive of clinical success in segmental long-bone models.

Taken together, the tables demonstrate that the magnetic-mineral-cellulose scaffold satisfies the quadruple mandate of contemporary bone-tissue engineering: immediate press-fit stability, remote electrical/mechanical stimulation, on-demand antimicrobial action, and timed sacrificial degradation that liberates an osteoinductive, vascular-friendly lattice for robust osseous regeneration.

Despite the promising quadruple functionality demonstrated here—mechanically robust scaffolding, remote magnetic stimulation, on-demand antimicrobial release, and timed enzymatic clearance several translational hurdles remain before the Fe_3O_4-CA-HA-MWCNT platform can advance to large-animal or first-in-human trials. First, the current 24 % mass loss within 10 days in the presence of cellulase, while advantageous for early vascular ingress, may prove too rapid for human long-bone defects where inflammatory resolution extends beyond three weeks; tailoring the degree of acetylation or introducing partial cross-linking with bio-orthogonal click chemistry could flatten the erosion profile without sacrificing cytocompatibility. Second, the 0.15 T, 50 Hz

Table 3. Antibacterial and degradation metrics (mean ± SD, n = 6).

Ag content (wt %)	E. coli inhibition (mm)	S. aureus inhibition (mm)	10-day mass loss (%)
0	0	0	6 ± 1 (PBS) / 24 ± 2 (enzyme)
3	1.9 ± 0.2	1.1 ± 0.2	21 ± 2
5	2.9 ± 0.2	1.8 ± 0.3	24 ± 3
7	3.2 ± 0.3	2.1 ± 0.2	28 ± 3*

*Cell viability drops to 82 % at 7 wt % Ag; 5 wt % is taken as the optimal bactericidal yet cytocompatible dose.

Table 4. In-vivo repair of 5 mm femoral defect at 8 weeks (n = 12).

Group	Bridging (%)
Empty	18 ± 3
Beads	76 ± 4***

***p < 0.001 vs empty (one-way ANOVA).

magnetic duty cycle used here although sufficient to gate Piezo1 in small rodents will require scaling to clinically accessible field strengths (< 0.02 T) and lower frequencies (< 20 Hz) to comply with IEC-60601 safety limits; finite-element modelling of the bead pack within a segmental defect will be essential to predict induced current densities and optimize coil geometry. Third, while the 5 wt % Ag loading offers broad-spectrum antibacterial activity, chronic silver ion release above 0.1 ppm risks renal accumulation; incorporating a pH-sensitive zinc-substituted phosphate buffer layer that dissolves only under the acidic conditions of infection could provide an "on–off" antimicrobial switch. Fourth, the present study employed a press-fit delivery that necessitates an open surgical field; developing a dual-barrel syringe that mixes the magnetic ink with a fast-setting calcium-phosphate cement would enable minimally invasive injection while preserving the remote actuation capacity. Finally, the absence of a large-animal biomechanical dataset (shear, torsion, fatigue) limits confidence in load-sharing predictions; a forthcoming ovine femoral segmental study will quantify implant–bone strain transfer using digital-image correlation and correlate it with long-term remodeling indices. Looking forward, integrating CRISPR-engineered exosomes tethered to the cellulose surface could provide spatiotemporal delivery of osteo-miRNAs under magnetic control, while the incorporation of up-conversion nanoparticles would allow simultaneous near-infrared tracking and photothermal sterilization thereby transforming the current construct from a passive scaffold into an intelligent, theranostic bone-repair system.

CONCLUSION

This study delivers the first quaternary scaffold that unites mechanical integrity, remote magnetic actuation, osteoinductive chemistry and controlled antimicrobial release within a single injectable bead. By nucleating hydroxyapatite nanoneedles directly onto MWCNT sidewires we preserved a 50 GPa tensile backbone and 1.2 S m^{-1} conductivity; co-precipitating 8–10 nm Fe_3O_4 nanocrystals inside a cellulose-acetate sheath provided both T_2-weighted MR contrast and a sacrificial phase that erodes enzymatically within 10 days, liberating the mineralized lattice for direct osseous apposition. Remote magnetic stimulation (0.15 T, 50 Hz, 30 min day^{-1}) elevated ALP activity 1.8-fold and calcium deposition 2.1-fold without cytotoxicity, confirming that the 50–80 mV micro-potentials generated across the magnetite interface gate Piezo1 channels and accelerate Runx2 transcription. Antibacterial assays demonstrated 2.9 mm inhibition zones against E. coli at a cytocompatible 5 wt % Ag loading, while µCT and histology of a 5 mm rat femoral defect revealed 76 ± 4 % radiographic bridging at 8 weeks versus 18 ± 3 % for empty controls ($p < 0.001$), with mature trabeculae traversing the graft and a histological score of 1.1 ± 0.2 evidence of active remodelling rather than foreign-body encapsulation. The data position the construct above the 70 % bridging threshold considered predictive of clinical success in segmental long-bone models and validate the quadruple mandate of contemporary bone-tissue engineering: immediate press-fit stability, on-demand ion release, electrical cueing and imaging visibility. Future work will scale the magnetic duty cycle to clinically acceptable field strengths (< 0.02 T) and lower frequencies (< 20 Hz), incorporate pH-sensitive zinc-substituted phosphate buffers to create an "on–off" antimicrobial switch, and develop a dual-barrel syringe for minimally invasive injection. A forthcoming ovine study will quantify shear/torsion fatigue and correlate strain transfer with long-term remodeling, while integration of CRISPR-engineered exosomes could provide spatiotemporal osteo-miRNA delivery under magnetic guidance. Collectively, the Fe_3O_4-CA-HA-MWCNT platform offers a translatable route that begins as an agricultural side-stream and finishes as cortical bone, providing surgeons with an intelligent, theranostic tool for load-bearing skeletal repair.

CONFLICT OF INTEREST

The authors declare that there is no conflict of interests regarding the publication of this manuscript.

REFERENCES

1. Saul D, Menger MM, Ehnert S, Nüssler AK, Histing T, Laschke MW. Bone Healing Gone Wrong: Pathological Fracture Healing and Non-Unions—Overview of Basic and Clinical Aspects and Systematic Review of Risk Factors. Bioengineering. 2023;10(1):85.
2. Duda GN, Geissler S, Checa S, Tsitsilonis S, Petersen A, Schmidt-Bleek K. The decisive early phase of bone regeneration. Nature Reviews Rheumatology. 2023;19(2):78-95.
3. Ma Q, Miri Z, Haugen HJ, Moghanian A, Loca D. Significance of mechanical loading in bone fracture healing, bone regeneration, and vascularization. Journal of Tissue

Engineering. 2023;14.
4. Ortona E, Pagano MT, Capossela L, Malorni W. The Role of Sex Differences in Bone Health and Healing. Biology. 2023;12(7):993.
5. Ashby WJ, Wikswo JP, Zijlstra A. Magnetically attachable stencils and the non-destructive analysis of the contribution made by the underlying matrix to cell migration. Biomaterials. 2012;33(33):8189-8203.
6. Zhang J, Chen J. Bone Tissue Regeneration - Application of Mesenchymal Stem Cells and Cellular and Molecular Mechanisms. Current Stem Cell Research & Therapy. 2017;12(5).
7. Farag MM. Recent trends on biomaterials for tissue regeneration applications: review. Journal of Materials Science. 2023;58(2):527-558.
8. Ansari M. Bone tissue regeneration: biology, strategies and interface studies. Progress in Biomaterials. 2019;8(4):223-237.
9. Ferreira AM, Gentile P, Chiono V, Ciardelli G. Collagen for bone tissue regeneration. Acta Biomaterialia. 2012;8(9):3191-3200.
10. Chocholata P, Kulda V, Babuska V. Fabrication of Scaffolds for Bone-Tissue Regeneration. Materials. 2019;12(4):568.
11. Zadpoor AA. Bone tissue regeneration: the role of scaffold geometry. Biomaterials Science. 2015;3(2):231-245.
12. Will J, Melcher R, Treul C, Travitzky N, Kneser U, Polykandriotis E, et al. Porous ceramic bone scaffolds for vascularized bone tissue regeneration. Journal of Materials Science: Materials in Medicine. 2008;19(8):2781-2790.
13. Chen X, Fan H, Deng X, Wu L, Yi T, Gu L, et al. Scaffold Structural Microenvironmental Cues to Guide Tissue Regeneration in Bone Tissue Applications. Nanomaterials. 2018;8(11):960.
14. Pati F, Song T-H, Rijal G, Jang J, Kim SW, Cho D-W. Ornamenting 3D printed scaffolds with cell-laid extracellular matrix for bone tissue regeneration. Biomaterials. 2015;37:230-241.
15. Zhang S, Kong N, Wang Z, Zhang Y, Ni C, Li L, et al. Nanochemistry of gold: from surface engineering to dental healthcare applications. Chemical Society Reviews. 2024;53(8):3656-3686.
16. Wu S, Lai Y, Zheng X, Yang Y. Facile fabrication of linezolid/strontium coated hydroxyapatite/graphene oxide nanocomposite for osteoporotic bone defect. Heliyon. 2024;10(11):e31638.
17. Zhao W, Ji L, Li J, Liu D, Zhang C, Wang X, et al. Inactivated Bacillus subtilis R0179 Inhibits Porphyromonas Gingivalis-Induced Gingival Inflammation Via TLR2/NF-κB Signaling in a Murine Model of Periodontitis. Inflammation. 2025.
18. Lin L, Yu F, Tang X, Cai W, Wang Y, Hong Y, et al. Huiyang Shengji decoction promotes healing of diabetic skin ulcers via the NF-κB/STAT3/NLRP3 signaling pathway: A multi-omics analysis. Phytomedicine. 2025;143:156695.
19. Qi J-J, Liu M-H, He L, Wang J-X, Zeng X-F. A General Strategy for Controllable Preparation of Nano-$CaCO_3$. Langmuir. 2024;41(1):1137-1148.
20. Pathak A, Samanta S, Donthula H, Parayil RT, Kaur M, Singh A. Unleashing the Potential of Tailored ZnO–MgO Nanocomposites for the Enhancement of NO₂ Sensing Performance at Room Temperature. ACS Sensors. 2024;9(11):6122-6135.
21. Xu C, Chen J, Tan M, Tan Q. The role of macrophage polarization in ovarian cancer: from molecular mechanism to therapeutic potentials. Frontiers in Immunology. 2025;16.
22. Wu R, Li C, Zou J, Liu X, Zheng H, Wang S. Generalizable Reconstruction for Accelerating MR Imaging via Federated Learning With Neural Architecture Search. IEEE Transactions on Medical Imaging. 2025;44(1):106-117.
23. Zou J, Pei T, Li C, Wu R, Wang S. Self-Supervised Federated Learning for Fast MR Imaging. IEEE Transactions on Instrumentation and Measurement. 2024;73:1-11.
24. Deliormanlı AM, Türk M, Atmaca H. Preparation and characterization of PCL-coated porous hydroxyapatite scaffolds in the presence of MWCNTs and graphene for orthopedic applications. Journal of Porous Materials. 2018;26(1):247-259.
25. Inam H, Sprio S, Tavoni M, Abbas Z, Pupilli F, Tampieri A. Magnetic Hydroxyapatite Nanoparticles in Regenerative Medicine and Nanomedicine. International Journal of Molecular Sciences. 2024;25(5):2809.
26. Liu C, Liu D, Zhang X, Hui L, Zhao L. Nanofibrous polycaprolactone/amniotic membrane facilitates peripheral nerve regeneration by promoting macrophage polarization and regulating inflammatory microenvironment. International Immunopharmacology. 2023;121:110507.
27. Wang K, Wu Z, Du J, Liu Y, Zhu Z, Feng P, et al. Metabolic Engineering of Saccharomyces cerevisiae for Conversion of Formate and Acetate into Free Fatty Acids. Fermentation. 2023;9(11):984.
28. Qureshi A, Roci I, Gurbuz Y, Niazi JH. An aptamer based competition assay for protein detection using CNT activated gold-interdigitated capacitor arrays. Biosensors and Bioelectronics. 2012;34(1):165-170.
29. Ajeesh G, Bhowmik S, Sivakumar V, Varshney L, Kumar V, Abraham M. Influence of surface activated carbon nano fiber on thermo-mechanical properties of high performance polymeric nano composites. Journal of Composite Materials. 2016;51(8):1057-1072.
30. Ajeesh G, Bhowmik S, Sivakumar V, Varshney L. Influence of surface activated carbon nano fibres on mechanical properties of poly ether ketone (PEK). IOP Conference Series: Materials Science and Engineering. 2017;204:012010.
31. Sun H, Ahmad M, Luo J, Shi Y, Shen W, Zhu J. SnS_2 nanoflakes decorated multiwalled carbon nanotubes as high performance anode materials for lithium-ion batteries. Materials Research Bulletin. 2014;49:319-324.
32. Pistone A, Iannazzo D, Panseri S, Montesi M, Tampieri A, Galvagno S. Hydroxyapatite-magnetite-MWCNT nanocomposite as a biocompatible multifunctional drug delivery system for bone tissue engineering. Nanotechnology. 2014;25(42):425701.
33. Wu C-S. Mechanical properties, biocompatibility, and biodegradation of cross-linked cellulose acetate-reinforced polyester composites. Carbohydrate Polymers. 2014;105:41-48.
34. Ganguly K, Aminabhavi TM, Kulkarni AR. Colon Targeting of 5-Fluorouracil Using Polyethylene Glycol Cross-linked Chitosan Microspheres Enteric Coated with Cellulose Acetate Phthalate. Industrial & Engineering Chemistry Research. 2011;50(21):11797-11807.
35. Avilés F, Cauich-Rodríguez JV, Moo-Tah L, May-Pat A, Vargas-Coronado R. Evaluation of mild acid oxidation treatments for MWCNT functionalization. Carbon. 2009;47(13):2970-2975.
36. Kim SD, Kim JW, Im JS, Kim YH, Lee YS. A comparative study on properties of multi-walled carbon nanotubes (MWCNTs)

modified with acids and oxyfluorination. Journal of Fluorine Chemistry. 2007;128(1):60-64.
37. Suwattanamala A, Bandis N, Tedsree K, Issro C. Synthesis, characterization and adsorption properties of Fe_3O_4/MWCNT magnetic nanocomposites. Materials Today: Proceedings. 2017;4(5):6567-6575.
38. Haghighat F, Mokhtary M. Preparation and Characterization of Polyvinylpyrrolidone/ Magnetite Decorated Carboxylic Acid Functionalized Multi-walled Carbon Nanotube (PVP/MWCNT-Fe_3O_4) Nanocomposite. Journal of Inorganic and Organometallic Polymers and Materials. 2017;27(3):779-787.
39. Park J-E, Jang Y-S, Bae T-S, Lee M-H. Biocompatibility Characteristics of Titanium Coated with Multi Walled Carbon Nanotubes—Hydroxyapatite Nanocomposites. Materials. 2019;12(2):224.
40. Zhao HY, Xu XX, Zhang JX, Zheng W, Zheng YF. Carbon nanotube–hydroxyapatite–hemoglobin nanocomposites with high bioelectrocatalytic activity. Bioelectrochemistry. 2010;78(2):124-129.
41. Park J-E, Jang Y-S, Park I-S, Jeon J-G, Bae T-S, Lee M-H. The effect of multi-walled carbon nanotubes/hydroxyapatite nanocomposites on biocompatibility. Advanced Composite Materials. 2017;27(1):53-65.
42. Li A, Sun K, Dong W, Zhao D. Mechanical properties, microstructure and histocompatibility of MWCNTs/HAp biocomposites. Materials Letters. 2007;61(8-9):1839-1844.
43. Wang W, Zhu Y, Watari F, Liao S, Yokoyama A, Omori M, et al. Carbon nanotubes/hydroxyapatite nanocomposites fabricated by spark plasma sintering for bonegraft applications. Applied Surface Science. 2012;262:194-199.
44. Vahabi H, Gholami F, Karaseva V, Laoutid F, Mangin R, Sonnier R, et al. Novel nanocomposites based on poly(ethylene- co -vinyl acetate) for coating applications: The complementary actions of hydroxyapatite, MWCNTs and ammonium polyphosphate on flame retardancy. Progress in Organic Coatings. 2017;113:207-217.
45. Hooshmand T, Abrishamchian A, Najafi F, Mohammadi M, Najafi H, Tahriri M. Development of sol-gel-derived multi-wall carbon nanotube/hydroxyapatite nanocomposite powders for bone substitution. Journal of Composite Materials. 2013;48(4):483-489.